Structural basis for GTP-induced dimerization and antiviral function of guanylate-binding proteins

Wen Cui[a,b,c,1], Elisabeth Braun[d,1], Wei Wang[c,1], Jinhong Tang[a,1], Yanyan Zheng[e,1], Benjamin Slater[f], Na Li[g], Cheng Chen[a], Qingxiang Liu[e], Bin Wang[a], Xiu Li[a], Yinkai Duan[b], Yunjie Xiao[a], Ruijiao Ti[a], Dominik Hotter[d], Xiaoyun Ji[c,h], Lei Zhang[a], Jun Cui[e], Yong Xiong[f], Daniel Sauter[d,i,2], Zefang Wang[a,j,2], Frank Kirchhoff[d,2], and Haitao Yang[a,b,j,2]

[a]School of Life Sciences, Tianjin University, Tianjin, 300072, China; [b]Shanghai Institute for Advanced Immunochemical Studies and School of Life Science and Technology, ShanghaiTech University, Shanghai, 201210, China; [c]Institute of Life Sciences, Chongqing Medical University, Chongqing, 400016, China; [d]Institute of Molecular Virology, Ulm University Medical Center, 89081 Ulm, Germany; [e]Key Laboratory of Gene Engineering of the Ministry of Education, State Key Laboratory of Biocontrol, School of Life Sciences, Sun Yat-sen University, 510006 Guangzhou, China; [f]Department of Molecular Biophysics and Biochemistry, Yale University, New Haven, CT 06520; [g]National Facility for Protein Science in Shanghai, Zhangjiang Lab, Shanghai Advanced Research Institute, Shanghai, 201210, China; [h]State Key Laboratory of Pharmaceutical Biotechnology, Department of Biotechnology and Pharmaceutical Sciences, School of Life Sciences, Nanjing University, Nanjing, 210023, China; [i]Institute for Medical Virology and Epidemiology of Viral Diseases, University Hospital Tübingen, Tübingen, 72076, Germany; and [j]Tianjin International Joint Academy of Biotechnology and Medicine, Tianjin, 300457, China

Edited by Hao Wu, Harvard Medical School, Boston, MA, and approved March 3, 2021 (received for review October 25, 2020)

Guanylate-binding proteins (GBPs) form a family of dynamin-related large GTPases which mediate important innate immune functions. They were proposed to form oligomers upon GTP binding/hydrolysis, but the molecular mechanisms remain elusive. Here, we present crystal structures of C-terminally truncated human GBP5 (hGBP5$_{1–486}$), comprising the large GTPase (LG) and middle (MD) domains, in both its nucleotide-free monomeric and nucleotide-bound dimeric states, together with nucleotide-free full-length human GBP2. Upon GTP-loading, hGBP5$_{1–486}$ forms a closed face-to-face dimer. The MD of hGBP5 undergoes a drastic movement relative to its LG domain and forms extensive interactions with the LG domain and MD of the pairing molecule. Disrupting the MD interface (for hGBP5) or mutating the hinge region (for hGBP2/5) impairs their ability to inhibit HIV-1. Our results point to a GTP-induced dimerization mode that is likely conserved among all GBP members and provide insights into the molecular determinants of their antiviral function.

innate immunity | guanylate-binding proteins | GTP-induced dimerization | antiviral factors | furin inhibition

Guanylate binding proteins (GBPs) are a family of interferon (IFN)-inducible guanosine triphosphatases (GTPases) that play important roles in innate immunity against diverse intracellular pathogens (1). Many GBPs show activities against bacterial and protozoan pathogens, such as *Toxoplasma gondii*, *Chlamydia trachomatis*, *Legionella*, and *Mycobacterium tuberculosis* (2). Some of them also have antiviral functions (3). Recently, human GBP5 (hGBP5) was found to restrict HIV-1 by interfering with the processing and incorporation of the viral envelope glycoprotein (Env) (4). A follow-up study revealed that hGBP5 and its paralogue hGBP2 suppress the activity of the virus-dependency factor furin, thereby inhibiting the proteolytic processing of the immature Env precursor gp160 into mature gp120 and gp41 required for virion infectivity (5). Furin is critical for proteolytic cleavage of many viral envelope proteins (6). In support of a key role in innate antiviral immunity, hGBP2 and hGBP5 also restrict other furin-dependent viruses, such as measles, Zika, and highly pathogenic avian influenza A viruses (5).

GBPs belong to the dynamin superfamily of large GTPases (7). These are characterized by an N-terminal large GTPase domain (LG domain) and one or more stalk domains (8), usually involved in oligomerization. The stalk domain of GBPs, which is also called C-terminal helical domain (CTHD), comprises the middle domain (MD) and GTPase effector domain (GED). It was proposed that GBPs undergo conformational changes and/or oligomerization upon GTP binding and hydrolysis (9), which may be important for their innate immune functions. Furthermore, GBP1, GBP2, and GBP5 are isoprenylated, and their membrane-binding abilities are modulated by the nucleotide state (10).

Despite the importance of this protein family in innate immunity and decades of research, their oligomerization mechanisms remain elusive due to limited structural data (11). The crystal structure of full-length human GBP1 (hGBP1^{FL}) was determined in its monomeric state (12). The crystal structure of the LG domain alone showed that it is able to form a dimer upon GTP binding (13). Based on these structures, a model of hGBP1^{FL} in the nucleotide-bound dimeric state was proposed, where the stalk domains protrude to the opposite direction, resulting in an "open" conformation (13). However, the accuracy of this model remains to be tested. Hence, the structures of full-length GBPs in their oligomeric state are in high demand to reveal the detailed molecular mechanisms of GBPs during innate immune responses.

Significance

Guanylate-binding proteins (GBPs) belong to interferon-inducible GTPases and mediate a broad spectrum of innate immune responses against various pathogens. Their protective functions require oligomerization induced by nucleotide binding and/or catalysis, but the actual molecular mechanisms are still elusive. Here, we report the crystal structures of human GBP5 (hGBP5) in both its nucleotide-free state and nucleotide-bound state, as well as nucleotide-free human GBP2 (hGBP2). We show that hGBP5 forms a closed face-to-face dimer upon GTP loading. This closed conformation is crucial to its anti–HIV-1 activity. Furthermore, with hGBP2 structure and SAXS validation, we propose a plausible working model for GTP-induced assembly of GBPs. Our findings lay the foundation to better understand the molecular mechanisms of GBPs and their immune functions.

Author contributions: L.Z., J.C., D.S., Z.W., F.K., and H.Y. designed research; W.C., E.B., J.T., Y.Z., B.W., X.L., R.T., and D.H. performed research; W.C., E.B., W.W., J.T., Y.Z., B.S., N.L., C.C., Q.L., B.W., Y.D., Y. Xiao, X.J., L.Z., J.C., Y. Xiong, D.S., Z.W., F.K., and H.Y. analyzed data; and W.C., E.B., W.W., Y.Z., X.J., D.S., Z.W., F.K., and H.Y. wrote the paper.

The authors declare no competing interest.

This article is a PNAS Direct Submission.

[1]W.C., E.B., W.W., J.T., and Y.Z. contributed equally to this work.

[2]To whom correspondence may be addressed. Email: Daniel.Sauter@med.uni-tuebingen.de, zefangwang@tju.edu.cn, frank.kirchhoff@uni-ulm.de, or yanght@shanghaitech.edu.cn.

This article contains supporting information online at https://www.pnas.org/lookup/suppl/doi:10.1073/pnas.2022269118/-/DCSupplemental.

Published April 5, 2021.

Here, we report the crystal structures of $hGBP5_{1–486}$ in both its nucleotide-free monomeric state and nucleotide-bound dimeric state, as well as full-length, nucleotide-free human GBP2 ($hGBP2^{FL}$). The structures of $hGBP5_{1–486}$ and $hGBP2^{FL}$ are similar to that of $hGBP1^{FL}$ in the absence of nucleotide. Upon nucleotide binding, however, the stalk domain of hGBP5 undergoes a drastic movement relative to the dimerized LG domain, resulting in a "closed" conformation entirely different from the previously proposed model. Two MD form a hydrophobic interface. Disrupting this interface or mutating the hinge region connecting LG domain and MD, reduces the anti–HIV-1 activity of hGBP2/5, suggesting a crucial role of the closed conformation in their antiviral function. Although the immune functions of the GBP family members are diverse and require specific signals, this dimerization mode is probably shared by all members of the family as revealed by small-angle X-ray scattering (SAXS). On these grounds, we propose a GTP-induced dimerization mechanism of GBPs which lays the foundation to understand the molecular bases of this important innate immune protein family.

Results

The Structure of Apo-hGBP5 Is Similar to That of hGBP1 without Nucleotide. To understand the conformational and/or oligomeric state change of GBPs that is important for their functions, it is necessary to determine the structures of GBP with and without nucleotide bound. We focused on hGBP5, since this IFN-inducible protein exerts broad antiviral activity (11). Full-length hGBP5 ($hGBP5^{FL}$) was susceptible to degradation in vitro. In contrast, $hGBP5_{1–486}$, comprising only the LG domain and MD, was more stable and amenable to crystallization. We were able to determine the crystal structure of $hGBP5_{1–486}$ in the absence of nucleotide at 3.0 Å (Fig. 1*A*). The final model comprises residues 1 to 486, with five poorly defined loop regions: $loop_{63–72}$, $loop_{101–107}$, $loop_{152–169}$, $loop_{183–192}$, and $loop_{239–255}$.

The structure of $hGBP5_{1–486}$ can be divided into three regions. The LG domain, which includes residues 6 to 295, forms a compact, globular domain, which comprises eight β-strands surrounded by eight α-helices. GTPases contain four motifs for GTP binding and hydrolysis, which are named G1 (P Loop), G2 (switch I), G3 (switch II), and G4 (N/TKxD motif) (14). These four motifs correspond to residues 45 to 54, 68 to 76, 97 to 112, and 179 to 182 of hGBP5, respectively. Moreover, the LG domains of GBPs harbor an additional region known as G5 (guanine cap, residues 239 to 260), which interacts with the guanine and the ribose of GTP. Residues 63 to 72, 101 to 107, 183 to 192, and 239 to 255 that are located close to these GTP-binding motifs are disordered in the absence of nucleotide. The LG domain in $hGBP5_{1–486}$ is very similar to that of $hGBP1^{FL}$ (Protein Data Bank [PDB]: 1DG3) (RMSD: 1.56 Å over 259 Cα atoms) (Fig. 1*B*). The MD of hGBP5 (residues 315 to 486) has an elongated shape (~90 Å) and comprises two three-helix bundles (3HB) with a shared long helix α9. Despite low sequence identity, superposing the MD of $hGBP5_{1–486}$ to that of $hGBP1^{FL}$ yields an RMSD of 2.4 Å over 162 Cα atoms.

The LG domain and MD of hGBP5 are connected by a hinge region, which comprises residues 295 to 315. The N-terminal half of this linker is part of α6, the last helix of the LG domain. The C-terminal half of the linker is part of α7, the first helix of the MD. It forms a sharp bend, stabilized by internally hydrophobic interactions (*SI Appendix*, Fig. S1). Although the arrangement of the LG domain and the MD in $hGBP5_{1–486}$ is similar to that in $hGBP1^{FL}$, alignment of the two structures by the LG domain shows a swing of the MD by 30° (*SI Appendix*, Fig. S1).

hGBP5 Forms a Face-to-Face Dimer Induced by Nucleotide Binding. Next, we determined the crystal structure of $hGBP5_{1–486}$ in complex with GDP · AlF_3 at 2.5 Å. A mutation of R356A was introduced at the hGBP5 surface as it enables the production of high-quality crystals without affecting the ability of hGBP5 to suppress HIV-1 Env processing or to reduce HIV-1 virion infectivity by inhibiting furin (*SI Appendix*, Fig. S2). $hGBP5_{1–486}$ forms a face-to-face dimer in complex with GDP · AlF_3 (Fig. 1*C*). In addition to a dimerization interface between the LG domains, the MDs also contact each other, further stabilizing the hGBP5 dimer. Interestingly, the hinge regions of $hGBP5_{1–486}$ cross one another, so that the stalk domain of one $hGBP5_{1–486}$ molecule is positioned beneath the LG domain of the pairing molecule (Fig. 1*C*).

We additionally solved the structure of the hGBP5 LG domain in complex with GDP · AlF_3 ($hGBP5^{LG}$), which is identical to the corresponding region in the dimer of $hGBP5_{1–486}$ (RMSD: 1.0 Å over 252 Cα atoms) (*SI Appendix*, Fig. S3) but determined at a higher resolution (2.3 compared to 2.5 Å).

The transition state analog, GDP · AlF_3 forms extensive interactions with the conserved nucleotide-binding motifs (Fig. 2*A*). G1 interacts with the phosphate groups in the nucleotide. Specifically, the backbone nitrogen atoms of S52 and Y53 in G1 form hydrogen bonds to α-phosphate oxygen atoms of GTP. The side chains of R48, K51, and S52 interact with β-phosphate oxygen. G2 and G3 play a crucial role in binding the γ-phosphate to distinguish GTP from GDP. In our structures, the backbone nitrogen atoms of T75 in G2 and G100 in G3 hydrogen bond to AlF_3, which mimics the γ-phosphate of GTP in the transition state. T75 coordinates a water molecule positioned 2.5 Å away from the AlF_3, functioning as nucleophilic agent. In addition, T75 and S52 coordinate a magnesium ion. This magnesium and R48 stabilize the negative charge accumulated in the transition state of GTP hydrolysis. In line with this, single mutations of R48, K51, S52, T75, and D182 to alanine result in a drastic decrease of GTPase activity (*SI Appendix*, Fig. S4).

The nucleotide stabilizes several regions located at the dimer interface, which explains why GTP binding is required for hGBP5 dimerization. For example, residues 62 to 72 and 101 to 106 become ordered when bound to GDP · AlF_3. These two regions are close to G2 and G3, which are directly involved in AlF_3 binding (Fig. 2*B*). S69, V71, and Q72 in G2 of one molecule form hydrogen bonds with G186 and D190, respectively, in G4 of the pairing molecule (Fig. 2*C*). G102, V104, and E105 in G3 interact with Q136, N202, and S203 of the pairing molecule. Moreover, the guanine cap of hGBP5, which is disordered without nucleotide, is stabilized and interacts with the same region of the other molecule (Fig. 2 *B* and *C*). The dimerization mode is very similar to that of hGBP1 (13) and buries an area of ~1,600 $Å^2$.

Although the GTP binding mode observed for hGBP5 is highly similar to that of hGBP1, some differences are observed. A conserved residue, S73, which serves as catalytic residue in hGBP1, does not coordinate the nucleophilic water in hGBP5 (Fig. 2*D*). Mutating S73 to alanine shows little effect on hGBP5 GTPase activity (*SI Appendix*, Fig. S4). Moreover, S69 forms a hydrogen bond to O3′ of the ribose in hGBP5 (Fig. 2*D*), while the same residue interacts with D188 from the pairing molecule at the dimer interface in hGBP1. These differences may account for the distinct hydrolytic ability of hGBP1 to generate GMP.

GTP Induces Drastic Movement and Dimerization of the MD. GTP induces a drastic conformation change in the hinge region, which has not been observed before. Superposing the hGBP5 structures in nucleotide-bound and nucleotide-free states by the LG domain shows a 90° swing of the MD (Fig. 3*A*). This large movement originates from rotation at a single residue D306 (Fig. 3*B*), which rotates around a Cα-C bond by 180° (Fig. 3*C*). Adjacent L307 and P308 do not show significant dihedral angle changes. The conformation rigidity of these residues may be required to translate the rotation around D306 to MD movement.

The rotated MD interacts with the LG domain and MD of the pairing molecule at two new interfaces, further stabilizing the hGBP5 dimer. At the hinge interface, V314, L317, E321, F371,

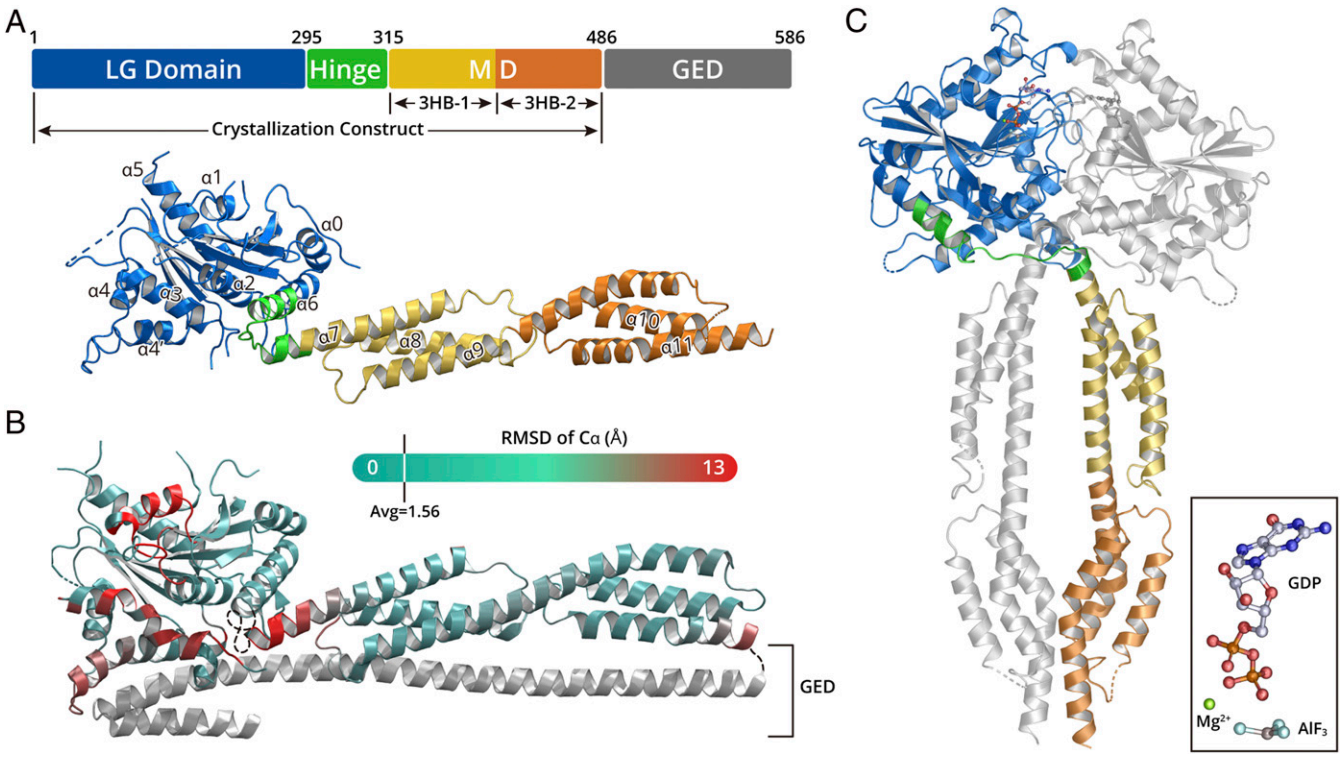

Fig. 1. hGBP5 structures in nucleotide-free and nucleotide-bound states. (*A*) A schematic representation and crystal structure of hGBP5 in its nucleotide-free state. LG domain, hinge region, MD, and GED are shown in blue, green, yellow/orange, and gray, respectively. (*B*) The structure of nucleotide-free hGBP1 (PDB: 1DG3) colored by RMSD from the structure of hGBP5 at Cα. The regions that show greatest deviation are depicted in red; the regions that show little deviation are depicted in cyan. The GED domain of hGBP1, which is missing in the hGBP5 structure, is shown in gray. (*C*) The crystal structure of hGBP5 in complex with GDP · AlF_3. The domains of one hGBP5 molecule are colored as those in *A*. The other molecule is shown in gray. The inset shows the structure of GDP · AlF_3 in the complex.

and K372 of the MD interact with H143, N144, E147, L148, L151, and R155 in α3 of the LG domain from the pairing molecule (Fig. 3*D*). Helices α3 and α4′ are extended in the presence of the MD in the dimer of $hGBP5_{1–486}$ compared to those in $hGBP5^{LG}$, agreeing with their role in mediating LG domain–MD interactions (*SI Appendix*, Fig. S3). Two MDs contact each other at the MD interface (Fig. 3*E*). This interface can be further divided into two parts (Fig. 3*E*). S465, K466, S468, V469, A472, T476, and A479 of α11 interact with the same residues from the pairing molecule by hydrophobic interactions and hydrogen bonds. These residues are located at the center of the interacting α11 helices and are named the inner interface. Moreover, K421 and E417 form additional interactions on both sides of the α11 pairs and are referred to as outer interface. These helices bundle together and bury a surface area of ∼740 $Å^2$.

The Closed Conformation Is Crucial for the Anti–HIV-1 Function of hGBP5. To test if the dimer interface between MDs plays an important role in restricting HIV-1, we designed a series of mutants to disrupt this interface. An hGBP5 mutant with all interacting residues at the MD interface mutated to alanine or glycine (MD dimerization mutant, MDDM) lacks anti–HIV-1 activity, just like hGBP1, which served as negative control (Fig. 4). hGBP5 restricts HIV-1 replication by suppressing proteolytic processing of the viral gp160 Env precursor into the functional surface gp120 and transmembrane gp41 units by the host protease furin. In line with this, the hGBP5 MDDM mutant lost its ability to inhibit the enzymatic activity of furin (Fig. 4*B*). Furthermore, hGBP5 MDDM does not markedly affect the ratio of mature processed gp120 to total Env protein levels (Fig. 4 *C* and *G*). To determine residues at the MD interface that play crucial roles in restricting HIV-1 replication, we mutated candidate residues in groups, based on their locations in the primary amino acid sequence (MDDM-A to MDDM-C) or the three-dimensional structure (MDDM-D to MDDM-F) (*SI Appendix*, Fig. S5). Combined substitution of E417 and K421 with alanines (MDDM-A) disrupted the antiviral activity of hGBP5 (Fig. 4*A*), while only moderately weakening its ability to inhibit furin activity and Env processing (Fig. 4 *B* and *C*). hGBP5 mutants MDDM-C, -E, and -F were less potent in impairing HIV-1 infectivity than MDDM-B and -D, although these five mutant forms showed little if any differences in their ability to inhibit furin and Env processing (Fig. 4 *A*–*C*).

Since the drastic conformational change of hGBP5 originates from its hinge region, modifying rigidity of this region may affect formation of the closed state. Although mutating D306, L307, or P308 to alanine individually (or D306 to proline) does not markedly reduce hGBP5's ability to impair HIV-1 infectivity, mutating all three residues together (D306A/L307A/P308A) completely abolishes this activity (*SI Appendix*, Fig. S6). Moreover, substituting L307 and P308 with alanine had little effect on hGBP5's ability to inhibit furin and proteolytic HIV-1 Env processing but decreased its ability to reduce anti–HIV-1 infectivity. This result suggests that hGBP5 restricts HIV-1 by genetically separable furin-dependent and -independent mechanisms (Fig. 4 *D*–*F* and *H*) and agrees with previous evidence that hGBP5 also affects *N*-linked glycosylation and trafficking of Env (4).

hGBP2 Shares a Similar Structure with hGBP5. Since the C-terminal isoprenylation site in the GED is crucial for hGBP5's antiviral activity (4, 5) (*SI Appendix*, Fig. S2), it is important to know the

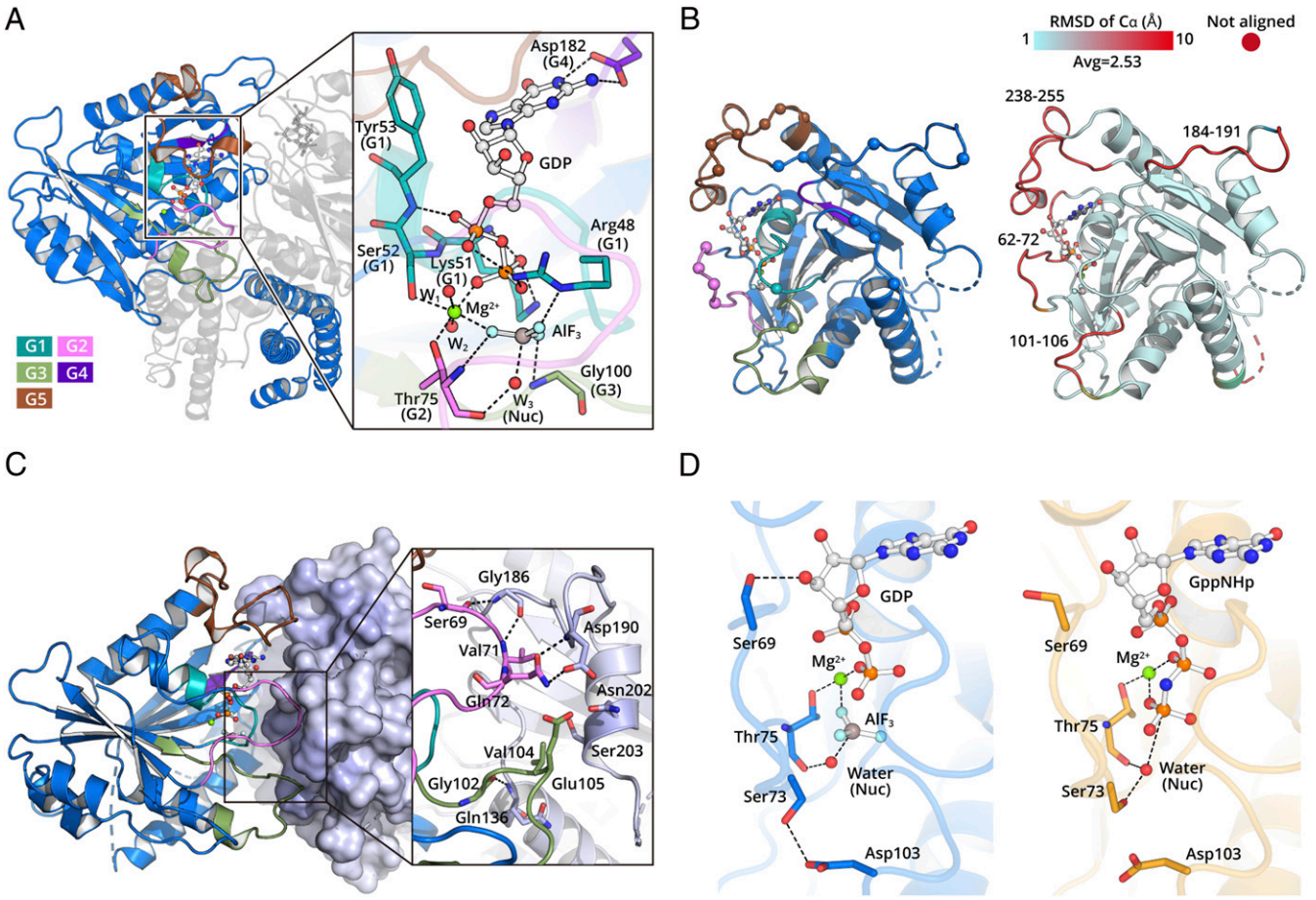

Fig. 2. The hGBP5 LG domain forms a dimer during GTP hydrolysis. (*A*) The hGBP5 LG domain binds GTP using canonical motifs depicted in different colors. The residues directly interacting with GDP · AlF_3 are shown as sticks. Hydrogen bonds are shown as black dotted lines. (*B*) LG domain dimer interface. Residues directly involved in intermolecular interactions are shown as spheres (*Left*). Conformational changes induced by nucleotide are colored by RMSD (*Right*). (*C*) The conserved nucleotide hydrolysis motifs are located at the LG domain dimer interface and directly mediate intermolecular interactions. A representative region at the interface is shown in the inset. (*D*) The nucleotide hydrolysis mode is slightly different between hGBP5 (*Left*) and hGBP1 (*Right*).

folding and conformation of this domain. hGBP2 and hGBP5 restrict HIV-1 replication by a similar mechanism (5). Thus, the structure of hGBP2's GED could serve as a useful model for that of hGBP5.

We therefore determined the structure of full-length hGBP2 ($hGBP2^{FL}$) in its nucleotide-free state at 2.6 Å (*SI Appendix*, Fig. S7*A*). The final model comprises all three domains: LG domain, MD, and GED. The LG domain has a compact, globular α/β structure, and the MD has an elongated shape comprising five helices. The structures of these domains are very similar to those of $hGBP5_{1–486}$ (RMSD 1.6 Å). The GED of hGBP2, which comprises two helices, contacts the LG domain through electrostatic interactions. A model of $hGBP2^{FL}$ in its nucleotide-bound state is proposed based on the structures of nucleotide-free $hGBP2^{FL}$ and $hGBP5_{1–486}$ in complex with GDP · AlF_3 (*SI Appendix*, Fig. S7*B*). The GEDs are predicted to be located at both sides of the $hGBP2^{FL}$ dimer.

The hinge region is crucial for hGBP2's anti–HIV-1 function. Mutating residues in the hinge region either alone (L307A and P308A) or in combination (L307A/P308A and D306A/L307A/P308A) almost completely abolishes hGBP2's ability to impair HIV-1 infectivity (Fig. 4 *D*–*F* and *H* and *SI Appendix*, Fig. S6).

GBPs Share a Conserved Dimerization Mode. To investigate if nucleotide-bound hGBP5 is in the closed state in solution, we collected SAXS data for both $hGBP5_{1–486}$ and $hGBP5^{FL}$ in the presence of GDP · AlF_3. The calculated curve using the crystal structure of dimeric $hGBP5_{1–486}$ is in line with the experimental data, yielding an χ^2 of 5.53 (Fig. 5 *A* and *B*). The presence of the GED does not seem to affect the overall conformation of hGBP5 (Fig. 5*C*). Considering the high sequence homology between hGBPs, we hypothesize that the GTP-induced dimerization mode observed for hGBP5 is conserved in other hGBPs. Indeed, the SAXS data of $hGBP1^{FL}$ and $hGBP2^{FL}$ with GDP · AlF_3 are highly similar to that of $hGBP5^{FL}$ (Fig. 5*C*), suggesting a common nucleotide-bound conformation.

An $hGBP5^{FL}$ model in the closed state fits the experimental data well, with an χ^2 of 21.0 (Fig. 5*D*). In contrast, the calculated SAXS curve based on a previously proposed model (13) in the open state deviates significantly from experimental data, yielding an χ^2 of 1,120. Taken together, the closed dimer represents a conserved GTP-induced dimerization mode of GBP family members, which may be critical for their immune functions.

Discussion

GBPs form a family of dynamin-like proteins (DLP). Despite the fact that this family was identified more than 30 y ago as one of the most prominent interferon-induced proteins with key roles in innate immunity, the precise molecular mechanisms remain elusive. Here, we show that GBPs undergo a drastic conformational change induced by GTP and form a face-to-face dimer. This "closed" dimer conformation seems to be conserved for the

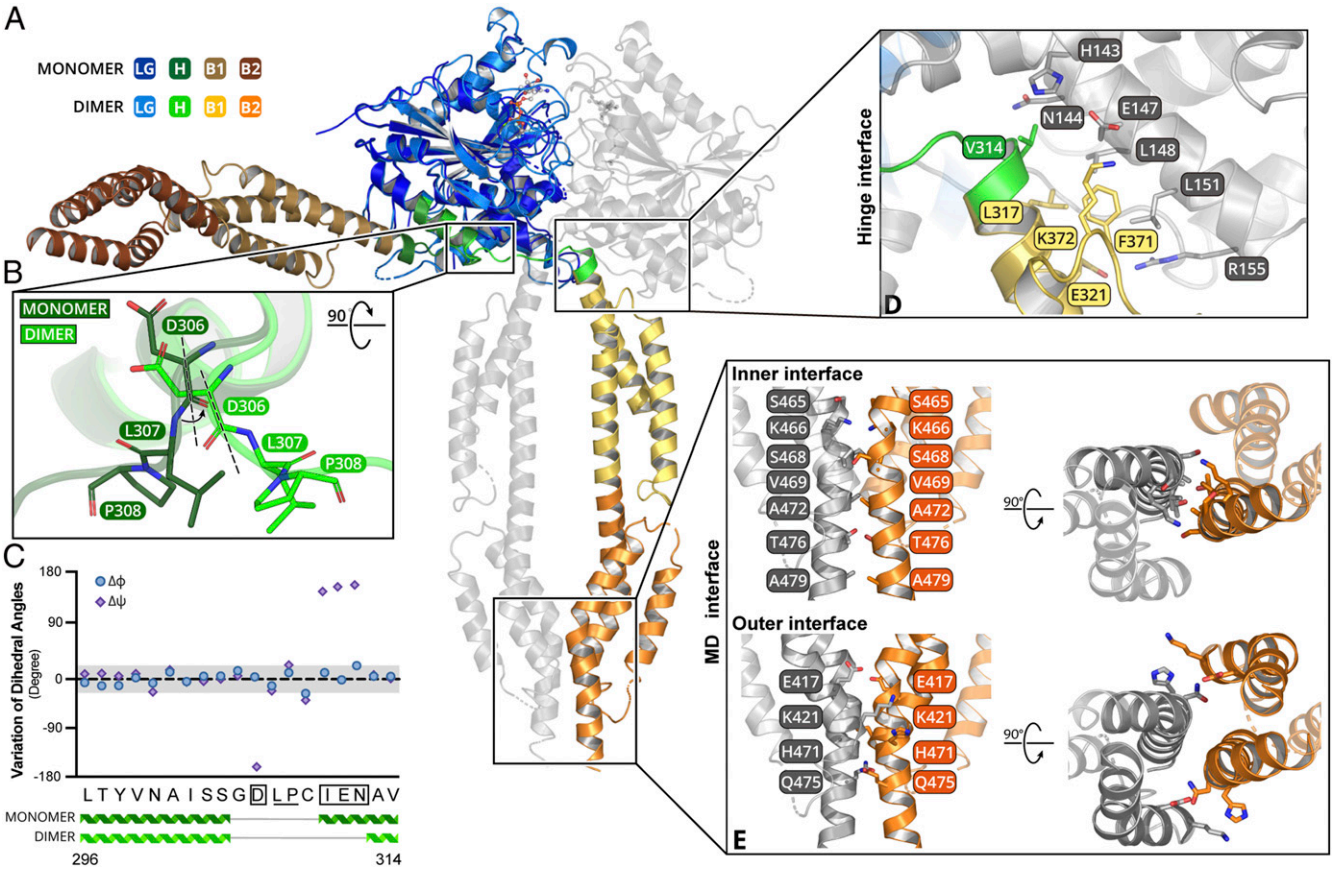

Fig. 3. The hGBP5 MD undergoes drastic movement and forms an extended dimer interface with GTP. (*A*) Superimposition of nucleotide-free and nucleotide-bound structures of hGBP5 reveals a drastic rearrangement of the MD. The color scheme is shown on the left. (*B*) The conformational change is due to a rotation in the hinge region. D306, L307, and P308 are shown as sticks. (*C*) Changes of the Cα dihedral angles of residues at the hinge region are plotted. (*D*) The hinge interface is shown in detail. The residues involved are shown as sticks. (*E*) The stalk interface can be divided into an inner interface and an outer interface. The residues involved are shown as sticks.

GBP family and is distinct from the previously proposed "open" conformation (13). Disrupting the MD interface (for hGBP5) or mutating the hinge region between LG domain and MD (for hGBP2/5) impairs their ability to inhibit HIV-1. The MD interface is crucial for furin inhibition. Thus, the "closed" conformation most likely represents the actual activated state of GBPs and is crucial for their antiviral and most likely other innate immune functions.

DLP activation is characterized by movement of stalk domains, which usually mediate DLP oligomerization (15). However, previously only movement of the GED has been observed for GBPs (16). Here, we demonstrate that GBP MDs also undergo significant conformational changes. Upon nucleotide binding, the MD of one molecule crosses over and positions beneath the LG domain of the other molecule, which originates from a conformational change at the hinge region and is stabilized by the MD dimer interface. This conformational change is most similar to that of atlastin (17), consistent with the fact that atlastin and GBPs are more closely related to each other than the rest of the DLP superfamily (18). Two other conformational switch modes have been observed in DLPs, where the stalk domains change between "closed" and "open" state but do not crossover (19). Whether there are other switch modes within the dynamin superfamily and how these modes are related to the origin and functions of DLPs warrants further study.

The antiviral function of hGBP2/5 was attributed to their ability to inhibit furin and consequently maturation of viral envelope glycoproteins (5). In this work, we show that the "closed" dimer conformation is required for this activity. Destabilizing the MD interface fully abrogates the antiviral effect of hGBP5. It has been shown that mutations in the catalytic site of hGBP5 have no marked effect on its anti–HIV-1 activity (4). One plausible explanation is that these mutants may still be able to bind GTP (20), which can induce hGBP5 dimerization (21) under certain circumstances (e.g., on Golgi membranes). In contrast, modifying the conformational rigidity of the hGBP2/5 hinge region also has an attenuating effect, independent of furin inhibition. This suggests that GBPs may also use furin-independent pathways to restrict viral replication (e.g., by altering Env glycosylation or trafficking) (4). Furin is exploited by numerous viral and bacterial pathogens (6). Recently, it was found that the spike protein of SARS-CoV-2 can be processed by furin, which has not been observed in other coronaviruses (22). Furin also cleaves cytokines, hormones, growth factors, and receptors, and its activity is associated with a variety of disorders including cancer (23). Thus, insights into the anti-furin determinants of hGBP2/5 have relevance beyond viral infection.

Membrane anchoring is a prerequisite for many functions of GBPs (11). GBPs can move to and disrupt the pathogen-containing vacuoles or bacteria membrane (24), which makes pathogen-associated molecular patterns exposed to cytoplasm and induces inflammation (25). They also need to localize to the Golgi to inhibit HIV-1 replication (5). This anchoring activity depends on CaaX isoprenylation and nucleotide-induced oligomerization (10). Based on our $hGBP5^{FL}$ dimer model, we proposed an anchoring mode resembling the Golgin-Arl1 complex (26). The Golgin-Arl1 complex is located at the Golgi membrane. It interacts with

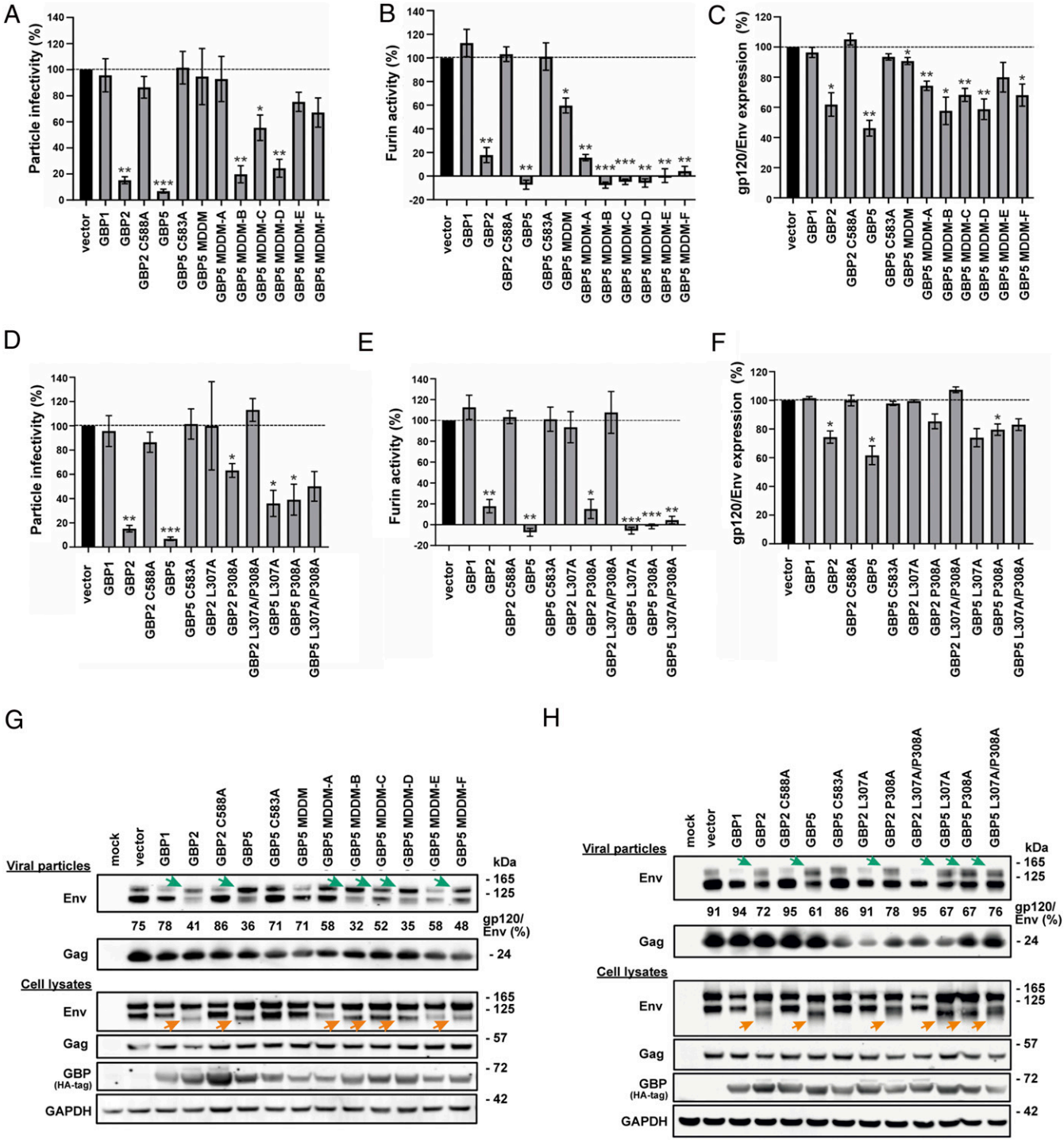

Fig. 4. Mutants in hinge region and MD dimer interface affect hGBPs antiviral activity. (*A*) HIV-1 particle infectivity, (*B*) furin activity, and (*C*) ratio of mature HIV-1 gp120 to total Env levels in the presence of hGBP5 mutants are determined in triplicate and plotted versus the vector control. The C588A and C583A variants represent previously characterized isoprenylation-deficient mutants of hGBP2 and hGBP5, respectively, that fail to restrict HIV-1 (5). They were included as negative controls. hGBP5 MDDM includes mutations E417A, K421A, K464A, S465A, K466A, S468A, V469A, H471A, A472G, Q475A, T476A, and A479G; MDDM-A includes mutations E417A and K421A; MDDM-B includes mutations K464A, S465A, K466A, S468A, and V469A; MDDM-C includes mutations H471A, A472G, Q475A, T476A, and A479G; MDDM-D includes mutations K464A, S465A, and K466A; MDDM-E includes mutations E417A, K421A, S468A, and H471A; MDDM-F includes mutations V469A, A472G, Q475A, T476A, and A479G. (*D*) HIV-1 particle infectivity, (*E*) furin activity, and (*F*) ratio of mature HIV-1 gp120 to total Env levels in the presence of hGBP2/hGBP5 hinge mutants are determined in triplicate and plotted versus the vector control. (*G* and *H*) Western blot analysis of HIV-1 Env and Gag in cells and viral particles when HEK293T cells were cotransfected with an HIV-1 proviral construct and hGBP dimer interface mutants (*G*) or hGBP hinge mutants (*H*). The green arrows indicate an increase of unprocessed Env (gp160) in viral particles. The orange arrows indicate a reduced apparent molecular weight of mature processed Env (gp120). No significance (ns): $P > 0.05$, $^{*}P \leq 0.05$, $^{**}P \leq 0.01$, and $^{***}P \leq 0.001$.

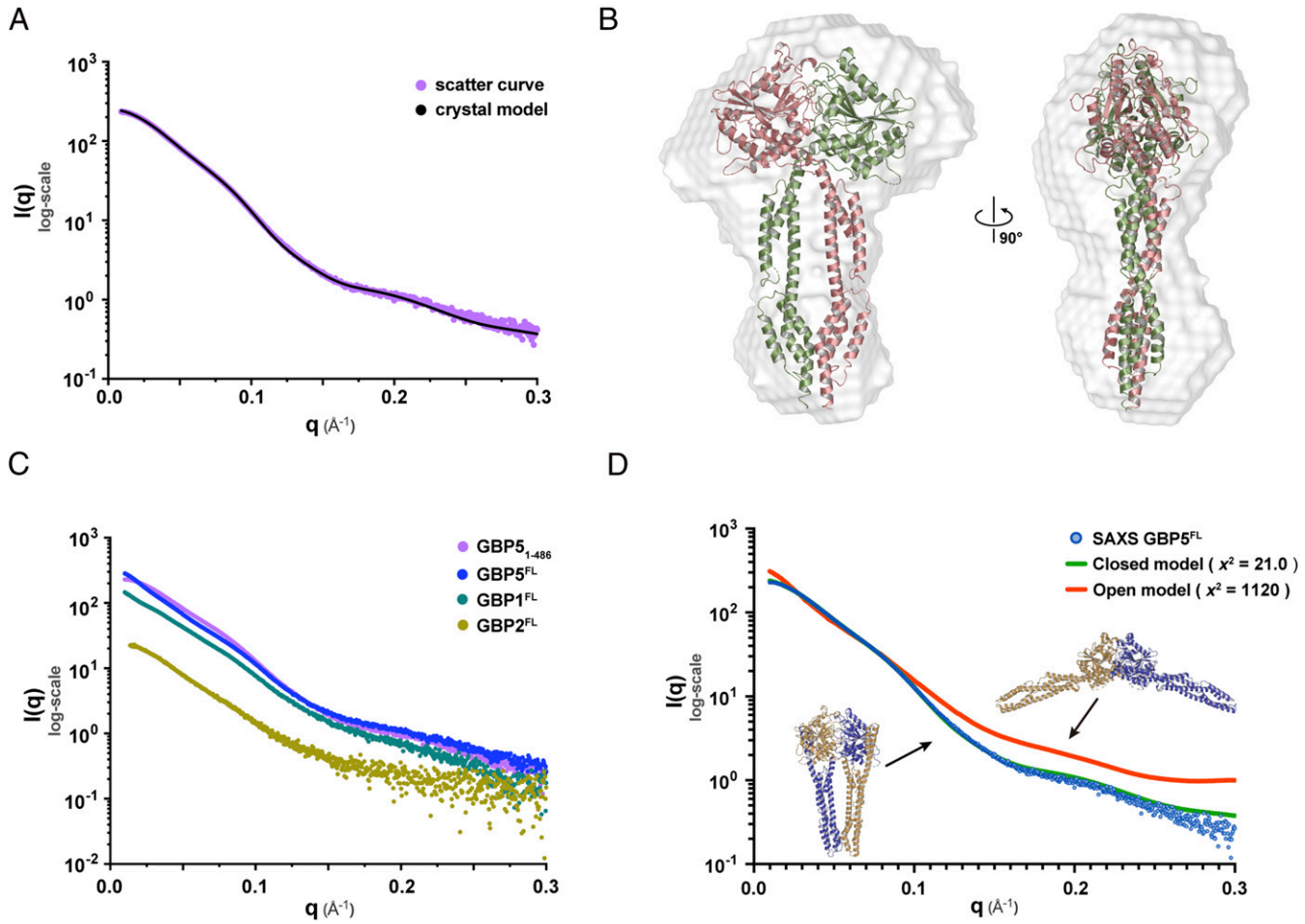

Fig. 5. Conserved dimerization mode of hGBPs. (*A*) The calculated scattering curve using the crystal structure of $hGBP5_{1–486}$ in complex with GDP · AlF_3 is in agreement with the SAXS data. (*B*) The crystal structure fits the SAXS envelope. (*C*) $hGBP1^{FL}$, $hGBP2^{FL}$, and $hGBP5^{FL}$ have similar scattering curves. (*D*) The SAXS data support a closed conformation of $hGBP5^{FL}$ in solution.

membranes using the CaaX motif next to the head and exposes the dimerized stalk domain for function. As for GBPs, upon nucleotide binding, α13 may become loose and detach from the LG domain so that the two isoprenylated regions are free to engage membranes. The dimerized stalk domain may function as a scaffold to recruit immunity-related GTPases, autophagy-related proteins (such as Atg4b and p62), NADPH oxidase subunits, and furin (27).

In conclusion, our study reveals an accurate and conserved GTP-induced dimerization mode of the GBP family. Based on this model, experiments can be designed to investigate how oligomerization and/or structural changes are related to the diverse functions of GBPs in host immunity. It could also serve as a starting point to characterize GBPs' interaction with other host proteins, membranes, and the formation of higher-order GBP assembly.

Materials and Methods

Cloning, Expression, and Purification. The coding sequences for $hGBP1^{FL}$, $hGBP2^{FL}$, and $hGBP5^{FL}$ were optimized and synthetized for *Escherichia coli* expression (Genewiz). The sequences encoding $hGBP1^{FL}$, $hGBP2^{FL}$, $hGBP5^{FL}$, $hGBP5_{1–486}$, and $hGBP5^{LG}$, which comprises residues 1 to 315 of hGBP5, were inserted into pET-28b using the *Bam*HI and *Xho*I restriction sites. A coding sequence for small ubiquitin-like modifier (SUMO) with 6× His-tag was inserted between restriction sites NcoI and *Bam*HI at the N-terminal of hGBPs to facilitate protein purification. Mutagenesis was performed using Easy site-directed mutagenesis kit (Transgen).

The expression plasmids were transformed into *E. coli* BL21 (DE3) and then cultured in Luria–Bertani broth containing 100 μg/mL kanamycin at 37 °C. When the cells were grown to an OD600 of ~0.6, 0.25 mM isopropyl β-D-thio-galactopyranoside was added to induce the expression at 16 °C. After 16 h, the cells were harvested by centrifugation at 3,000 × *g*. The cell pellet was resuspended in lysis buffer (50 mM Tris HCl pH 8.0, 500 mM NaCl, 20 mM imidazole, 5 mM $MgCl_2$, and 10% glycerol), lysed by high-pressure homogenization, and then centrifuged at 20,000 × *g* for 40 min. The supernatant was then loaded onto nickel-nitrilotriacetic acid affinity resin (GE Healthcare) to capture the 6× His-SUMO–tagged target protein in lysate. After washing with the resuspension buffer, the target protein was eluted by cleavage buffer (50 mM Tris HCl pH 8.0, 100 mM NaCl, 150 mM imidazole, 5 mM $MgCl_2$, and 10% glycerol), and SUMO tag was removed by adding SUMO protease (ULP) and incubating at 4 °C for 18 h. The target protein was then purified by sequentially ion exchange chromatography (HiTrap Q, GE Healthcare) and size-exclusion chromatography (Superdex 200, GE Healthcare). The purified protein was stored in storage buffer (20 mM Tris HCl pH 8.0, 5 mM $MgCl_2$, and 1 mM dithiothreitol [DTT]) at −80 °C.

GTPase Activity Assay. The GTPase activity assay was performed as described previously (28) using QuantiChrom ATPase/GTPase Assay Kit (BioAssay Systems). Briefly, hGBP (at 2 μM) was incubated with 1 mM of GTP in reaction buffer (40 mM Tris pH 7.5, 80 mM NaCl, 8 mM $Mg(Ac)_2$, and 1 mM ethylenediaminetetraacetic acid (EDTA)) at 25 °C for 20 min. At the end of the reaction, the concentration of free phosphate produced was determined by measuring absorbance at 620 nm and interpolating to a standard curve. The reaction rate was calculated by dividing the amount of phosphate produced by reaction time and plotted with Prism (GraphPad).

Crystallization, Data Collection, and Structure Determination. All crystals were grown by the microbatch-under-oil method.

hGBP5$_{1–486}$ was crystallized at 12 °C by mixing 1 μL protein (5 mg/mL) with 1 μL crystallization buffer containing 4% Tacsimate pH 5.0 and 12% wt/vol Polyethylene glycol 3350 (Hampton Research). The cryo-protectant solution contained 4% Tacsimate pH 5.0, 12% wt/vol polyethylene glycol 3350, and 15% glycerol. Diffraction data were collected at 100 K at Shanghai Synchrotron Radiation Facility (SSRF) beamline BL18U1 at a wavelength of 0.97853 Å. Data integration and scaling were performed using HKL3000 (29). The structure was solved by molecular replacement with PHASER (30) using the structure of hGBP1 (PDB: 1F5N) as a search model. Multiple rounds of model building in COOT (31) and refinement in PHENIX (32) were performed. COOT and PyMOL (Schrödinger) were used for the structural analysis and illustration.

hGBP5$_{1–486}$ in complex with GDP · AlF_3 was crystallized at 12 °C by mixing 1 μL protein–nucleotide complex (6 mg/mL hGBP5$_{1–486}$ with 5 mM $MgCl_2$, 5 mM $AlCl_3$, 60 mM NaF, and 5 mM GDP) and 1 μL crystallization buffer containing 0.2 M ammonium sulfate, 0.1 M *N*-2-hydroxyethylpiperazine-*N*-ethane-sulphonicacid (HEPES) pH 7.5, and 25% wt/vol polyethylene glycol 3350. The cryo-protectant solution contained 0.2 M ammonium sulfate, 0.1 M HEPES pH 7.5, 25% wt/vol polyethylene glycol 3350, and 15% glycerol. Diffraction data were collected at 100 K at SSRF beamline BL18U1 at a wavelength of 0.97852 Å. Data integration and scaling were performed using HKL3000. The structure was determined by molecular replacement with PHASER using the structure of hGBP1 (PDB: 1F5N) as a search model. Model building and refinement were performed as described above.

hGBP5^{LG} in complex with GDP · AlF_3 was crystallized at 12 °C by mixing 1 μL protein–nucleotide complex (5 mg/mL hGBP5^{LG} with 5 mM $MgCl_2$, 5 mM $AlCl_3$, 60 mM NaF, and 5 mM GDP) and 1 μL crystallization buffer containing 0.2 M sodium formate pH 7.0 and 20% wt/vol polyethylene glycol 3350. The crystals were cryoprotected by Paratone oil (Hampton Research). Diffraction data were collected at 100 K at SSRF beamline BL18U1 at a wavelength of 0.97879 Å, and the structure was solved by molecular replacement with PHASER using the structure of hGBP1 (PDB: 2B92) as a search model.

hGBP2^{FL} was crystallized at 23 °C by mixing 1 μL protein (8 mg/mL) with 1 μL crystallization buffer containing 15% vol/vol 2-propanol, 0.1 M sodium citrate, tribasic dihydrate pH 5.0, and 10% wt/vol polyethylene glycol 10,000 (Hampton Research). The cryo-protectant solution contained 15% vol/vol 2-propanol, 0.1 M sodium citrate, tribasic dihydrate pH 5.0, 10% wt/vol polyethylene glycol 10,000, and 15% glycerol. Diffraction data were collected at 100 K at SSRF beamline BL18U1 at a wavelength of 0.97853 Å. Process of diffraction data processing, model building, and refinement were performed as described above.

Data collection and structure refinement statistics are summarized in *SI Appendix*, Table S1.

SAXS. SAXS experiments were performed at beamline BL19U2 of National Center for Protein Science Shanghai at SSRF. The wavelength, λ, of X-ray radiation was set as 1.033 Å. Scattered X-ray intensities were collected using a Pilatus 1 M detector (DECTRIS Ltd,). The sample-to-detector distance was set such that the detecting range of momentum transfer [$q = 4\pi \sin\theta/\lambda$, where 2θ is the scattering angle] of SAXS experiments was 0.01 to 0.30 Å^{-1}. To reduce the radiation damage, a flow cell made of cylindrical quartz capillary with a diameter of 1.5 mm and a wall thickness of 10 μm was used. Measurements were carried out at three different concentrations (i.e., 1 mg/mL, 3 mg/mL, and 5 mg/mL) and SAXS data were collected at 10 °C using 60 μL sample in incubation buffer (20 mM Tris HCl pH 8.0, GDP 7.2 mM, $AlCl_3$ 5 mM, $MgCl_2$ 10 mM, NaF 60 mM, and 1 mM DTT) as 20 × 1 s exposures. Scattering profiles for 20 exposure were compared to exclude data showing radiation damage and averaged. The two-dimensional scattering images were converted to one-dimensional SAXS curves through azimuthally averaging after solid angle correction and then normalizing by the intensity of the transmitted X-ray beam using the software package BioXTAS RAW (33). Background scattering was subtracted using PRIMUS in ATSAS software package (34). Linear Guinier plots in the Guinier region ($q*R_g < 1.3$) were confirmed in all experimental groups. Pair distance distribution functions of the particles P(r) and the maximum sizes D_{max} were computed using GNOM (35), and molecular weights were estimated by empirical estimation based on the average excluded volume deduced from the SAXS model. The ab initio shapes were determined using DAMMIF (36) with 15 DAMMIF runs for each experimental group, and DAMAVER (37) was used to analyze the normalized spatial discrepancy (NSD) between the 15 models. The model with the lowest NSD was shown.

Cloning of pCG Expression Plasmids. pCG expression plasmids for N-terminal HA-tagged human GBP1, GBP2, and GBP5 as well as GBP2 C588A and GBP5 C583A were already available and described previously (5). Most additional hGBP2 and hGBP5 mutants were generated via conventional mutagenesis PCR using wild-type expression plasmids as template. Cloning into a pCG expression vector coexpressing blue fluorescent protein via an internal ribosome entry site was performed using unique XbaI and MluI restriction sites. Residue D306 was mutated using the Q5 Site-Directed Mutagenesis Kit (NEB) according to the manufacturer's instructions. To facilitate detection of the hGBPs, an N-terminal HA-tag (TACCCATACGATGTTCCAGATTACGCT) was introduced via the forward PCR primer. All constructs were sequenced to verify their integrity. PCR primers are listed in *SI Appendix*, Table S2.

Western Blotting and Virus Releases Assays. HEK293T cells (provided and authenticated by the American Type Culture Collection) were seeded in a 6-well plate format in a density of 6 × 10^5 cells per well 1 d prior to transfection. Cells were cotransfected with an expression plasmid for the indicated hGBPs (1.5 μg) and a proviral construct for HIV-1 CH058 (2.5 μg). Cells and supernatants were harvested 40 h posttransfection.

To determine cellular and viral proteins, cells were washed in phosphate-buffered solution (PBS), lysed in Western Blot lysis buffer (150 mM NaCl, 50 mM HEPES, 5 mM EDTA, 0.1% Nonidet P-40, 500 mM Na_3VO_4, and 500 mM NaF, pH 7.5) and cleared by centrifugation at 20,800 × *g* for 20 min at 4 °C. Lysates were mixed with protein sample loading buffer (LI-COR) (22.5%) and β-mercaptoethanol (2.5%) and heated at 95 °C for 5 min. Virions from cell culture supernatants were purified via a sucrose cushion. Briefly, 250 μL of 20% sucrose were overlaid with 700 μL virus-containing cell culture supernatant and centrifuged at 20,800 × *g* for 90 min at 4 °C. Subsequently, supernatants were discarded and 10 μL Western Blot lysis buffer (75% supplemented with 25% protein sample loading buffer and 2.5% β-mercaptoethanol) was added and heated at 95 °C for 5 min. Proteins were separated using 4 to 12% NuPAGE Novex Bis-Tris gels (Invitrogen) and blotted onto Immobilon-FL Transfer polyvinylidene difluoride membranes (Merck Millipore). Cellular and viral proteins were stained using primary antibodies directed against HA-tag (Abcam, #ab18181), GAPDH (BioLegend, #631401), HIV-1 Env (obtained through the NIH AIDS Reagent Program, Division of AIDS, The National Institute of Allergy and Infectious Diseases (NIAID), NIH: 16H3 mAb from Barton F. Haynes and Hua Xin Liao) (38), p24 (Abcam, #ab9071), and infrared dye–labeled secondary antibodies (LI-COR). Proteins were detected using an infrared LI-COR Odyssey Imager and band intensities were quantified using Image Studio Lite Version 4.0 (LI-COR).

To determine infectious virus yield, TZM-bl reporter cells (provided and authenticated by the NIH AIDS Reagent Program, Division of AIDS, NIAID, NIH from John C. Kappes, Xiaoyun Wu, and Tranzyme Inc.) (39) were seeded in a 96-well plate format in a density of 6,000 cells per well 1 d prior to infection. TZM-bl reporter cells were infected in triplicates with 5 to 100 μL cell culture supernatants. Three days postinfection, cells were lysed and β-galactosidase reporter gene expression was determined using the GalScreen Kit (Applied Biosystems/Life Technologies) according to the manufacturer's instructions.

To determine the amount of virus particles present in cell culture supernatants, the p24 capsid protein was quantified in a homemade p24 sandwich ELISA. High-binding ELISA plates (Sarstedt) were coated with an anti-p24 coating antibody (ExBio, #11-CM006-BULK) overnight at room temperature. Plates were washed, blocked with 10% fetal calf serum in PBS for 2 h at 37 °C. Virus particles present in the cell culture supernatant were lysed in 1% Triton X-100 for 1 h at 37 °C and diluted in PBS supplemented with 0.05% Triton X-100 and 0.05% Tween-20. Diluted samples and a serially diluted p24 protein standard (Abcam, #43037) were transferred to the ELISA plates. After overnight incubation, plates were washed, incubated with anti-p24 serum (Eurogentec) followed by incubation with an horseradish peroxidase-conjugated secondary antibody (Dianova, #111-035-008), each for 1 h at 37 °C. Plates were washed again and tetramethylbenzidine substrate (SeraCare Life Sciences) was added and incubated for 20 to 30 min at room temperature before the reaction was stopped with 0.5 M H_2SO_4. Absorption was measured at 450 nm with a baseline correction at 650 nm using a VMax kinetic ELISA microplate reader (Molecular Devices). p24 concentrations were determined by using the software SoftMax Pro (Molecular Devices). Infectious virus yield was normalized to the amount of viral particles (p24) to calculate particle infectivity.

Furin Activity Assay. HEK293T cells were seeded in a 6-well plate format in a density of 6 × 10^5 cells per well 1 d prior to transfection. Cells were cotransfected with an expression plasmid for the indicated hGBPs (1.5 μg) and an expression plasmid for human furin (0.25 μg). Cells were harvested 40 h posttransfection, washed with PBS, lysed in amido-4-methylcoumarin (AMC) lysis buffer (500 mM HEPES, 5 mM $CaCl_2$, 5 mM β-mercaptoethanol, and 2.5% Triton X-100, pH 7.0) and cleared by centrifugation at 20,800 × *g* for 20 min at 4 °C. High-binding ELISA plates (Sarstedt) were coated with an anti-furin antibody (R&D Systems, #AF1503) or an isotype control antibody (R&D Systems, #AB-108-C) (50 μL/well at 10 μg/mL) overnight at room temperature. Plates

were washed, blocked in PBS supplemented with 0.5% sucrose and 0.5% tween-20 and washed again before cell lysates were added and incubated overnight at 4 °C. Plates were washed and incubated with Pyr-Arg-Thr-Lys-Arg-7-AMC substrate (Bachem, #I-1650) (1 nmol), and furin activity was determined for 60 min using a Cytation3 imaging reader (355 nm excitation and 460 nm emission). The area under the curve was calculated, the background was subtracted, and the empty vector control was set to 100%.

Statistical Analysis. Student's *t* tests were performed to compare GTP-hydrolysis activity between wild-type hGBP5 and mutants. The GTPase activity of each mutant was compared to that of wild-type hGBP5 using unpaired *t* test. Particle infectivity, furin activity, and gp120/Env expression in the presence of hGBP1/2/5 and mutants were compared to the vector control using one-sample *t* test.

Data Availability. The PDB accession codes for the coordinates of $hGBP5_{1–486}$, $hGBP5_{1–486}$ in complex with GDP · AlF_3, $hGBP5^{LG}$ in complex with GDP · AlF_3, and $hGBP2^{FL}$ are 7E59, 7E5A, 7CKF, and 7E58, respectively. All other study data are included in the article and/or *SI Appendix*.

ACKNOWLEDGMENTS. We thank Henry Nguyen for assistance. We are grateful to National Centre for Protein Science Shanghai and College of Life Sciences, ShanghaiTech University for use of their instrumentation and technical assistance. We also thank the staff from beamlines BL17U1, BL18U1, BL19U1, and BL19U2 at Shanghai Synchrotron Radiation Facility (China). This work was supported by grants from the National Key Research Program of China (2016YFD0500300) to L.Z. and X.J., the National Natural Science Foundation of China (81772204), the Natural Science Foundation of Tianjin (18JCJQJC48000) to H.Y., and the National Natural Science Foundation of China (81902063) to W.W. This work was also supported by grants from the German Research Foundation (F.K.: CRC 1279, SPP 1923, and KI 548/16-1; D.S.: SPP 1923 and the Heisenberg Programme), the German Federal Ministry of Education and Research (protACT, 01KI20135 to D.S.), and the Baden-Württemberg foundation to F.K.

1. G. J. K. Praefcke, Regulation of innate immune functions by guanylate-binding proteins. *Int. J. Med. Microbiol.* **308**, 237–245 (2018).
2. B.-H. Kim *et al*., Interferon-induced guanylate-binding proteins in inflammasome activation and host defense. *Nat. Immunol.* **17**, 481–489 (2016).
3. B. H. Kim, A. R. Shenoy, P. Kumar, C. J. Bradfield, J. D. MacMicking, IFN-inducible GTPases in host cell defense. *Cell Host Microbe* **12**, 432–444 (2012).
4. C. Krapp *et al*., Guanylate binding protein (GBP) 5 is an interferon-inducible inhibitor of HIV-1 infectivity. *Cell Host Microbe* **19**, 504–514 (2016).
5. E. Braun *et al*., Guanylate-binding proteins 2 and 5 exert broad antiviral activity by inhibiting furin-mediated processing of viral envelope proteins. *Cell Rep.* **27**, 2092–2104.e10 (2019).
6. E. Braun, D. Sauter, Furin-mediated protein processing in infectious diseases and cancer. *Clin. Transl. Immunology* **8**, e1073 (2019).
7. R. Ramachandran, S. L. Schmid, The dynamin superfamily. *Curr. Biol.* **28**, R411–R416 (2018).
8. J. R. Jimah, J. E. Hinshaw, Structural insights into the mechanism of dynamin superfamily proteins. *Trends Cell Biol.* **29**, 257–273 (2019).
9. S. Shydlovskyi *et al*., Nucleotide-dependent farnesyl switch orchestrates polymerization and membrane binding of human guanylate-binding protein 1. *Proc. Natl. Acad. Sci. U.S.A.* **114**, E5559–E5568 (2017).
10. N. Britzen-Laurent *et al*., Intracellular trafficking of guanylate-binding proteins is regulated by heterodimerization in a hierarchical manner. *PLoS One* **5**, e14246 (2010).
11. K. Tretina, E.-S. Park, A. Maminska, J. D. MacMicking, Interferon-induced guanylate-binding proteins: Guardians of host defense in health and disease. *J. Exp. Med.* **216**, 482–500 (2019).
12. B. Prakash, G. J. K. Praefcke, L. Renault, A. Wittinghofer, C. Herrmann, Structure of human guanylate-binding protein 1 representing a unique class of GTP-binding proteins. *Nature* **403**, 567–571 (2000).
13. A. Ghosh, G. J. K. Praefcke, L. Renault, A. Wittinghofer, C. Herrmann, How guanylate-binding proteins achieve assembly-stimulated processive cleavage of GTP to GMP. *Nature* **440**, 101–104 (2006).
14. A. Wittinghofer, I. R. Vetter, Structure-function relationships of the G domain, a canonical switch motif. *Annu. Rev. Biochem.* **80**, 943–971 (2011).
15. O. Daumke, G. J. K. Praefcke, Invited review: Mechanisms of GTP hydrolysis and conformational transitions in the dynamin superfamily. *Biopolymers* **105**, 580–593 (2016).
16. A. S. Piro *et al*., Detection of cytosolic *Shigella flexneri* via a C-terminal triple-arginine motif of GBP1 inhibits actin-based motility. *MBio* **8**, e01979-17 (2017).
17. L. J. Byrnes, H. Sondermann, Structural basis for the nucleotide-dependent dimerization of the large G protein atlastin-1/SPG3A. *Proc. Natl. Acad. Sci. U.S.A.* **108**, 2216–2221 (2011).
18. J. Hu *et al*., A class of dynamin-like GTPases involved in the generation of the tubular ER network. *Cell* **138**, 549–561 (2009).
19. M. G. J. Ford, J. S. Chappie, The structural biology of the dynamin-related proteins: New insights into a diverse, multitalented family. *Traffic* **20**, 717–740 (2019).
20. G. J. K. Praefcke *et al*., Identification of residues in the human guanylate-binding protein 1 critical for nucleotide binding and cooperative GTP hydrolysis. *J. Mol. Biol.* **344**, 257–269 (2004).
21. S. Ince, M. Kutsch, S. Shydlovskyi, C. Herrmann, The human guanylate-binding proteins hGBP-1 and hGBP-5 cycle between monomers and dimers only. *FEBS J.* **284**, 2284–2301 (2017).
22. D. Bestle *et al*., TMPRSS2 and furin are both essential for proteolytic activation of SARS-CoV-2 in human airway cells. *Life. Sci. Alliance* **3**, e202000786 (2020).
23. S. Tian, Q. Huang, Y. Fang, J. Wu, D. B. Furin, FurinDB: A database of 20-residue furin cleavage site motifs, substrates and their associated drugs. *Int. J. Mol. Sci.* **12**, 1060–1065 (2011).
24. M. P. Wandel *et al*., Guanylate-binding proteins convert cytosolic bacteria into caspase-4 signaling platforms. *Nat. Immunol.* **21**, 880–891 (2020).
25. C. C. Ngo, S. M. Man, Mechanisms and functions of guanylate-binding proteins and related interferon-inducible GTPases: Roles in intracellular lysis of pathogens. *Cell. Microbiol.* **19** (2017).
26. M. Wu, L. Lu, W. Hong, H. Song, Structural basis for recruitment of GRIP domain golgin-245 by small GTPase Arl1. *Nat. Struct. Mol. Biol.* **11**, 86–94 (2004).
27. S. Huang, Q. Meng, A. Maminska, J. D. MacMicking, Cell-autonomous immunity by IFN-induced GBPs in animals and plants. *Curr. Opin. Immunol.* **60**, 71–80 (2019).
28. H. Tian *et al*., Structural basis of Zika virus helicase in recognizing its substrates. *Protein Cell* **7**, 562–570 (2016).
29. Z. Otwinowski, W. Minor, Processing of X-ray diffraction data collected in oscillation mode. *Methods Enzymol.* **276**, 307–326 (1997).
30. A. J. McCoy *et al*., Phaser crystallographic software. *J. Appl. Cryst.* **40**, 658–674 (2007).
31. P. Emsley, B. Lohkamp, W. G. Scott, K. Cowtan, Features and development of coot. *Acta Crystallogr. D Biol. Crystallogr.* **66**, 486–501 (2010).
32. P. D. Adams *et al*., PHENIX: A comprehensive python-based system for macromolecular structure solution. *Acta Crystallogr. D Biol. Crystallogr.* **66**, 213–221 (2010).
33. S. S. Nielsen *et al*., BioXTAS RAW, a software program for high-throughput automated small-angle X-ray scattering data reduction and preliminary analysis. *J. Appl. Cryst.* **42**, 959–964 (2009).
34. M. V. Petoukhov *et al*., New developments in the *ATSAS* program package for small-angle scattering data analysis. *J. Appl. Cryst.* **45**, 342–350 (2012).
35. D. I. Svergun, Determination of the regularization parameter in indirect-transform methods using perceptual criteria. *J. Appl. Cryst.* **25**, 495–503 (1992).
36. D. Franke, D. I. Svergun, *DAMMIF*, a program for rapid *ab-initio* shape determination in small-angle scattering. *J. Appl. Cryst.* **42**, 342–346 (2009).
37. V. V. Volkov, D. I. Svergun, Uniqueness of ab initio shape determination in small-angle scattering. *J. Appl. Cryst.* **36**, 860–864 (2003).
38. F. Gao *et al*., Cross-reactive monoclonal antibodies to multiple HIV-1 subtype and SIVcpz envelope glycoproteins. *Virology* **394**, 91–98 (2009).
39. E. J. Platt, K. Wehrly, S. E. Kuhmann, B. Chesebro, D. Kabat, Effects of CCR5 and CD4 cell surface concentrations on infections by macrophagetropic isolates of human immunodeficiency virus type 1. *J. Virol.* **72**, 2855–2864 (1998).